Electrooxidation of hydrazine hydrate using Ni–La catalyst for anion exchange membrane fuel cells

Tomokazu Sakamoto [a,*], Koichiro Asazawa [a], Ulises Martinez [b], Barr Halevi [b], Toshiyuki Suzuki [c], Shigeo Arai [c], Daiju Matsumura [d], Yasuo Nishihata [d], Plamen Atanassov [b], Hirohisa Tanaka [a]

[a] Frontier Technology R & D Division, Daihatsu Motor Co., Ltd., 3000 Yamanoue, Ryuo, Gamo, Shiga 520-2593, Japan
[b] Chemical & Nuclear Engineering Department, UNM Center for Emerging Energy Technologies, University of New Mexico, Albuquerque, NM 87131, USA
[c] High Voltage Electron Microscope Laboratory, Ecotopia Science Institute, Nagoya University, Furo-cho, Chikusa-ku Nagoya 464-8603, Japan
[d] Quantum Beam Science Directorate, Japan Atomic Energy Agency, 1-1-1 Koto, Sayo, Hyogo 679–5148, Japan

HIGHLIGHTS

► Ni–La/C catalysts were synthesized and investigated for hydrazine oxidation.
► The $Ni_{0.9}La_{0.1}$/C catalyst exhibited the best onset potential and mass activity.
► HVEM suggested the metal particles are composed of Ni cores with Ni_xLa_y shells.

ABSTRACT

Carbon supported Ni, La, and $Ni_{1-x}La_x$ ($0.1 \leq x \leq 0.9$) catalysts were synthesized by an impregnation/freeze-drying procedure followed by thermal annealing. The catalytic activity for electro-oxidation of hydrazine hydrate on anionic ionomer-coated catalysts was evaluated using a (4×4) 16-channel electrochemical electrode array in 1.0 M KOH + 1.0 M hydrazine hydrate solution at 60 °C. The $Ni_{0.9}La_{0.1}$/C catalyst oxidized hydrazine hydrate at a lower potential and exhibited higher mass activity in comparison with a similarly made Ni/C catalyst. Chemical insight suggests that the cause of improved performance for the $Ni_{0.9}La_{0.1}$/C catalyst is likely multifunctional synergism of the components. However, X-ray absorption fine structure (XAFS) and high voltage electron microscopy (HVEM) unexpectedly show some hcp–$LaNi_5$ shells coating the fcc–Ni catalyst particles. As a result of the screening tests, an unsupported $Ni_{0.9}La_{0.1}$ catalyst was synthesized by spray pyrolysis and tested in a direct hydrazine hydrate fuel cell MEA (DHFC) producing 453 mW cm^{-2}.

© 2013 Elsevier B.V. All rights reserved.

1. Introduction

H_2/O_2 polymer electrolyte fuel cells (PEFCs), which use proton exchange membranes as electrolytes, have been intensively developed as a primary power source for fuel cell vehicles (FCVs) in an effort to reduce fossil fuel dependence. However, to become commercially viable PEFCs have to overcome cost and availability barriers caused by the reliance on Pt and Pt-based catalysts in both anode and cathode electrodes of FCs. The need for onboard hydrogen storage in vehicles also hinders the popularization of FCVs. Onboard hydrogen storage for a 500 km range requires the use of a high pressure tank of 70 MPa of hydrogen, presenting both a technological barrier and a major safety hazard.

In contrast with H_2/O_2 PEFCs which use proton exchange membranes, anionic polymer electrolyte fuel cells can use less expensive electrocatalysts that are based on transition metals due to the less corrosive environment inherent to alkaline systems. Also, liquid-feed fuel cell systems offer many benefits over hydrogen fuel systems because hydrogen is difficult to transport and store while the current fuel transportation infrastructure is for fluids. Different liquid fuels have therefore been studied for direct liquid automotive and portable fuel cells with different technologies relying on ethanol (DEFCs) [1], methanol (DMFCs) [2], ammonia (DAFCs) [3], borohydride (DBFCs) [4] and hydrazine hydrate (DHFCs). Recent developments in Hydrazine-Hydrate fuel cell technology have led to full-sized demonstration DHFCs indicating their feasibility and promise in future fuel cell vehicles [5–8].

* Corresponding author. Tel.: +81 748 1685; fax: +81 748 57 1064.
E-mail addresses: tomokazu_sakamoto@mail.daihatsu.co.jp, tomokazu.sakamoto@gmail.com (T. Sakamoto).

When selecting a fuel for FCVs it is of course necessary to consider safety, physical characteristic, and theoretical performance data for the specific application. Table 1 shows a summary of factors relevant for evaluating FCV fuels for the three fuels 100% hydrazine hydrate ($N_2H_4 \cdot H_2O$), anhydrous hydrazine (N_2H_4), and hydrogen (H_2). Because of widely held views on hydrazine safety, it is important to note that hydrazine hydrate has completely different properties from anhydrous hydrazine. Hydrazine hydrate is industrially used as a chemical reagent, with approximately 20,000 tons/year of hydrazine hydrate distributed in Japan regularly. Hydrazine hydrate has a freezing temperature of −50 °C which means it can be used as fuel in FCVs in cold regions and it is less volatile than alcohol fuels so that air emissions are lower. The flame point of 100% hydrazine hydrate is 74 °C at atmospheric pressure, however, at concentrations less than 60%, hydrazine hydrate is not flammable. The carcinogenic risk of hydrazine hydrate, class 2B by International Agency for Research on Cancer (IARC) report, is equivalent gasoline so careful handling of the fuel is required but not more so than currently accepted guidelines for gasoline. The relative carcinogenic safety of hydrazine is illustrated by carcinogenicity studies that found no increased cancer risk for workers in a hydrazine production plant [9,10]. As a fuel hydrazine hydrate has several benefits including safety, efficiency, and energy density as reported by W. Qian et al. [11]. Hydrazine hydrate electrooxidation leads to harmless N_2 and H_2O products, and the theoretical efficiency of DHFCs is higher than H_2/O_2 PEFCs. Further, the liquid fuel used in DHFCs has a higher energy density than H_2, and the theoretical potential of DHFCs (1.62 V) is also superior to DEFCs (1.15 V), DMFCs (1.21 V), and DAFCs (1.17 V), except for DBFCs (1.64 V), when O_2 is used for a cathode fuel [12]. Thus, hydrazine hydrate presents an attractive alternative to hydrogen for FCVs.

Electrodes for hydrazine electrooxidation reactions have been studied as early as 1960's [13–15], and much effort has been devoted to the development of new electrocatalysts for hydrazine electrooxidation for DHFCs [16–23]. We previously reported that the electrocatalytic activity of Ni and Co is higher than Pt for electrooxidation of hydrazine hydrate in alkaline environments [24]. In recent research Ni-based binary alloy catalysts such as Ni–Zn [25,26], Ni–Co [27,28], Ni–Pd [29], Ni–Ag [30], Ni–Pt [31], Ni–Zr [7], and Ni–Fe [32] were shown to improve hydrazine hydrate oxidation efficiently through alloying effects. These improved performance levels motivated us to further study Ni-alloy catalysts for use in DHFCs. Other complex catalysts were also developed for hydrazine oxidation and hydrazine derivatives oxidation including [(bpy)$_2$Ru(5−phenNH$_2$)]Cl$_2$·H$_2$O (byp; bipyridine, phen; phenanthroline) and Co porphyrin [33,34]. Despite improvements to date, hydrazine oxidation catalysts must be further improved to meet the required catalytic activity and selectivity for the popularization of DHFCVs.

The Ni–La binary system contains various intermetallic crystal structures such as LaNi$_5$, LaNi [35] which are known to be active hydrogen absorption materials and therefore can be projected to have good hydrogen activation performance. In this study we therefore synthesized, characterized, and tested carbon supported $Ni_{1-x}La_x$ ($0.1 \leq x \leq 0.9$) catalysts for hydrazine hydrate oxidation in alkaline media. The results of this investigation identified $Ni_{0.9}La_{0.1}$/C as the best formulation and conjectures on the active phase are reported. The optimal formulation was then used to develop unsupported catalysts, and we present preliminary results for an unsupported $Ni_{0.9}La_{0.1}$ catalyst tested in a direct hydrazine hydrate fuel cell MEA (DHFC) producing 453 mW cm^{-2}.

2. Experimental

2.1. Catalyst synthesis

2.1.1. Impregnation/freeze-drying procedure for the catalyst screening

Ni/C, La/C, $Ni_{1-x}La_x$/C catalysts were synthesized using an impregnation/freeze-drying procedure followed by thermal annealing for the screening test. The atomic composition (as at%) of each sample was varied in 10 at% increments from (90:10) to (10:90). All catalysts samples contained 23 wt% total metal on carbon support. First, aqueous metal nitrate solutions made from precursor compounds of $Ni(NO_3)_2 \cdot 6H_2O$ (98%, Kishida Chemical) and $La(NO_3)_2 \cdot 6H_2O$ (97%, Kishida Chemical) dissolved in deionized water (>18.2 MΩ cm, Millipore Direct−Q 3 UV Water Purification System, Millipore) were impregnated with carbon black (Ketjenblack ECP600JD, Lion) by a robotic liquid dispenser (Model GX271, Gilson) utilized to pipette the desired amount of metal solution. Slurries were sonicated for 5 min and the impregnated catalysts were then immersed in liquid N_2. The cooled slurries were freeze-dried under a moderate vacuum (0.055 mbar, FreeZone, Labconco) over 40 h. All catalysts were prepared in 10 mL quartz vials. Reduction of metal precursors to the zero-valent state on the carbon support was thermally driven under a reductive H_2 atmosphere (10% H_2, balance Ar) at 250 °C for 2.5 h using a tube furnace. Final thermal annealing was performed immediately after the reduction step at 800 °C for 5 h in 10% H_2 atmosphere.

2.1.2. Spray pyrolysis for MEA anode catalyst

Synthesis of unsupported $Ni_{0.9}La_{0.1}$ catalyst was achieved using spray pyrolysis following a previously reported approach [25,26]. Metal nitrates (Ni and La) (99%, Sigma−Aldrich Co.) were dissolved

Table 1

Comparison of hydrazine hydrate ($N_2H_4 \cdot H_2O$), anhydrous hydrazine (N_2H_4), and hydrogen (H_2) properties. Including physical properties at 25 °C/1 atm, virulence, reaction equations, thermochemical data ($-\Delta H$; Enthalpy, $-\Delta G$; Gibbs free energy), theoretical potential (E^0), efficiency (ε), and energy density.

	100% hydrazine hydrate ($N_2H_4 \cdot H_2O$)	Anhydrous hydrazine (N_2H_4)	Hydrogen (H_2)
Major use	Blowing agent Deoxidizer Reductant	Rocket fuel Aircraft fuel –	Petroleum synthesis Weld Reductant
Physical condition	Liquid	Liquid	Gas
Freezing point	−51.7 °C	2 °C	−259 °C
Boiling point	121 °C	114 °C	−253 °C
Flame point	74 °C	38 °C	−157 °C
Possibly carcinogenic to humans by IARC	2B	2B	–
Toxicology (Rat)	LD50 = 129 mg kg^{-1}	LD50 = 60 mg kg^{-1}	Blackdamp
Electrochemical reaction	N_2H_4 (l) + O_2(g) → N_2(g) + 2H_2O (l)		2H_2(g) + O_2(g) → 2H_2O (l)
$-\Delta H$	622 kJ mol^{-1}		286 kJ mol^{-1}
$-\Delta G$	623 kJ mol^{-1}		237 kJ mol^{-1}
E^0	1.62 V		1.23 V
ε	100%		83%
Energy density	5.4 kWh L^{-1}		0.18 kWh L^{-1} (7 MPa)

in 10% HNO_3 solution to a final concentration of 5% of specific stoichiometric ratios. The dissolved bimetallic solution was atomized (Model 3076, TSI Inc.) and pyrolyzed through a furnace at 700 °C using N_2 as the carrier gas. Pyrolyzed particles were collected on a Teflon filter and air dried. Alloys were formed by reduction of the oxide powders under 5% H_2 in N_2 at 500 °C.

2.2. Evaluation of catalytic activity

2.2.1. Electrochemical measurement using a (4 × 4) 16-channel electrochemical electrode array

Catalyst inks were prepared in the following manner. 10 mg of the desired catalyst was combined with 7.5 mL of DI water, 1.5 mL of isopropanol, 0.46 mL of THF and 0.04 mL of a 5 wt% anionic ionomer solution (A3, Tokuyama). The ink was then sonicated during 15 min. After sonication, 0.04 mL of the ink was applied onto the GC electrode, resulting in a loading of 0.054 mg cm^{-2}. The entire array was then left to dry for at least 1 h.

A (4 × 4) 16-channel electrochemical electrode array for parallel testing of prepared electrocatalysts was utilized in this study. This equipment for the catalyst screening is a modified version of an array previously used by K. C. Neyerlin et al. [36]. The array consisted of mirror polished glassy carbon working electrodes where the different catalyst materials were applied. Each of these electrodes was in contact with independent samples of the testing solution, and independently controlled by multi-potentiostat (1470E, Solartron Analytical). Due to the use of strong alkaline media, a Zn/ZnO quasi reference electrode was utilized instead of the conventional Hg/HgO reference electrode. The reference electrode consisted in a Zn wire immersed in 1.0 M KOH solution. A Pt wire served as counter electrode. All potentials presented and discussed here are reported against a reversible hydrogen electrode (RHE) at pH 14.

2.2.2. Measurement of DHFCs

100 mg of the catalyst was combined with 0.96 mL of isopropanol, 0.24 mL of THF and 0.2 mL of a 5 wt% anionic ionomer solution (A3, Tokuyama). The ink was then sonicated 5 min. After sonication, ZrO_2 beads (Diameter = 2.0 mm, Nikkato) were added and the mixture was agitated for 15 min. The prepared ink was directly sprayed onto an anionic electrolyte membrane (A201, Tokuyama). Co-PPY-C (PPY: polypyrrole, Hokko Chemical Industry) cathode catalyst was formed into an electrode using a similar method to that for the cathode. The membrane was then pressed for 5 min at room temperature to bind the catalyst layers to the membrane. The membrane was then immersed in 1.0 M KOH solution for 8 h in order for the ion-exchange to OH$^-$ form of the anionic membrane.

The prepared MEA, with a round shaped working electrode area of 1 cm^2, was inserted in a single cell to measure the cell performance. The fuel of 1.0 M KOH + 20% $N_2H_4 \cdot H_2O$ was supplied to the anode at flow rate of 2 mL min^{-1}, and oxygen gas humidified at 50 °C was supplied to the cathode at the flow rate of 500 mL min^{-1}. The applied shape of the flow-fields was serpentine for the anode and comb-shaped for the cathode. The cell temperature was controlled at 80 °C. The differential operating pressures on both anode and cathode sides were 20 kPa.

2.3. Characterization of catalysts

The crystal structures of the prepared catalysts were examined using the $\theta-2\theta$ X-ray diffraction (XRD, RINT 2000, Rigaku) with the Cu Kα source of operating at a potential of 40 kV and a current of 450 mA. 2θ diffraction angles ranged from 10° to 110° at 5° min^{-1}. X-ray absorption fine structure (XAFS) measurements of samples

mixed with boron nitride were carried out at BL14B2 of SPring−8 in Japan with transmission mode at room temperature. Transmission electron microscope (TEM, H−800, Hitachi) with the voltage acceleration of 200 kV and energy dispersive X-ray spectroscopy (EDX, 550I, Kevex) were performed to analyze catalyst morphology and composition. High Voltage Electron Microscopy (HVEM) was carried out on two 1000 kV microscopes (HVEM, H−1250ST, Hitachi and JEM−1000K RS, JEOL) to investigate the surface structure of catalysts.

3. Results and discussion

3.1. Catalyst survey using a (4 × 4) 16-channel electrochemical electrode array

Fig. 1 shows the linear sweep voltammetry (LSV) profiles of Ni/C, La/C, and Ni$_{1-x}$La$_x$/C ($0.1 \leq x \leq 0.9$) catalysts which were prepared by an impregnation/freeze-drying procedure. A (4 × 4) 16−channel electrochemical electrode array was used to evaluate the catalytic activity for hydrazine oxidation from −0.129 V to 0.221 V in 1 M KOH + 1 M hydrazine hydrate electrolyte at 60 °C, and results were summarized in Table 2. The onset potential is defined as the potential at 10.9 A g^{-1}, and mass activity is defined as the current per unit total metal weight at 0.221 V vs. RHE. The anodic peaks in the potential range from 0 V to 0.221 V vs. RHE are ascribed to hydrazine oxidation as shown in Fig. 1. La/C has no catalytic activity for hydrazine oxidation in this potential range, while samples with more than 70at% Ni had the lowest onset potential and highest mass activity. Ni$_{0.9}$La$_{0.1}$/C and Ni$_{0.8}$La$_{0.2}$/C show higher hydrazine oxidation catalytic activity than the Ni/C catalyst at 0.221 V vs. RHE. The mass activity of Ni$_{0.9}$La$_{0.1}$/C and Ni$_{0.8}$La$_{0.2}$/C are 759.5 A·g^{-1} and 477.5 A·g^{-1} respectively, which are 2.2 and 1.4 times higher than that Ni/C, as shown in Table 2. The inset of Fig. 1 illustrates the best onset potential, where Ni$_{0.9}$La$_{0.1}$/C has an onset potential of −0.0464 V vs. RHE which is 0.0419 V lower than Ni/C. The mass activity at a low potential is more representative of catalyst intrinsic performance and depends on the surface structure of catalysts, because charge-transfer rate is considered slow at a low potential [37]. All the onset potentials and mass activities listed in Table 2 are plotted in Fig. 2. From Fig. 2 it is clear that the onset potential improves with Ni addition. The mass activity rises sharply from 0 to 10 at % La added, decreases from 10 to 30 at %, and then remains nearly constant across the remainder of the La content range. The maximum hydrazine oxidation mass activity was observed for Ni$_{0.9}$La$_{0.1}$/C indicating an intrinsically different catalytic performance for Ni$_{0.9-0.7}$La$_{0.1-0.3}$/C than that of the catalysts containing more Lanthanum.
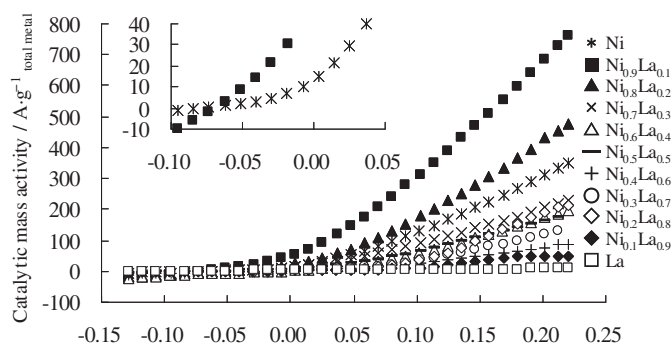

Fig. 1. LSV profiles of prepared Ni/C, La/C, and Ni$_{1-x}$La$_x$/C ($0.1 \leq x \leq 0.9$) catalysts at scanning rate of 20 mV s^{-1}.

Table 2
Catalytic activity of prepared Ni/C, La/C, and $Ni_{1-x}La_x$/C ($0.1 \leq x \leq 0.9$) using a (4×4) 16-channel electrochemical electrode array.

| Catalyst	Onset potential at 10.9 A g^{-1} (V vs. RHE)	Mass activity at 0.221 V vs. RHE (A g^{-1})
Ni/C	−0.0045	350.2
$Ni_{0.9}La_{0.1}$/C	−0.0464	759.5
$Ni_{0.8}La_{0.2}$/C	−0.0194	477.5
$Ni_{0.7}La_{0.3}$/C	−0.0045	231.3
$Ni_{0.6}La_{0.4}$/C	0.0326	197.1
$Ni_{0.5}La_{0.5}$/C	0.0185	185.4
$Ni_{0.4}La_{0.6}$/C	0.0516	88.6
$Ni_{0.3}La_{0.7}$/C	0.0516	141.5
$Ni_{0.2}La_{0.8}$/C	0.0625	214.5
$Ni_{0.1}La_{0.9}$/C	0.0966	48.9
La/C	−	9.1

3.2. The cell performance of DHFCs

Fig. 3 shows the cell performances of DHFCs using $Ni_{0.9}La_{0.1}$ as an anode catalyst, together with conventional Ni catalyst (210H, INCO) as a reference catalyst. Co-PPY-C was used as a cathode catalyst. The results of MEA evaluation are summarized in Table 3. The DHFCs showed high performance without precious metal catalysts on either anode or cathode, as shown in Fig. 3. When Ni and $Ni_{0.9}La_{0.1}$ were used as anode catalysts in DHFCs, their open circuit voltages (OCV) were observed 0.746 V and 0.751 V, respectively. The difference in observed OCV between Ni and $Ni_{0.9}La_{0.1}$ relate to the improved onset potential for hydrazine oxidation when La is added to Ni, or possibly the structure of the catalyst layer in the MEA. The maximum power density for $Ni_{0.9}La_{0.1}$ is 453 mW cm^{-2} is 14% higher than the 397 mW cm^{-2} obtained for the pure Ni catalyst. The improved performance of the unsupported $Ni_{0.9}La_{0.1}$ catalyst when compared to the Ni confirms the results of the carbon supported $Ni_{1-x}La_x$ ($0.1 \leq x \leq 0.9$) catalysts where the $Ni_{0.9}La_{0.1}$/C formulation was the best performing anode catalyst for DHFCs. To better understand the cause of the improved performance of $Ni_{0.9}La_{0.1}$/C extensive characterization was carried out as described later in this manuscript. Also, more extensive studies of the unsupported $Ni_{1-x}La_x$ made by spray pyrolysis were made and will be reported shortly.

3.3. XRD analysis

To obtain insight on the crystal structure of the prepared Ni/C, La/C, and $Ni_{1-x}La_x$/C ($0.1 \leq x \leq 0.9$) materials XRD analysis was performed from 10° to 110° as shown in Fig. 4. The broad peaks near the 25° and 60° observed in all samples are attributed to the carbon support. The diffraction peaks of Ni/C and $Ni_{1-x}La_x$/C ($0.1 \leq x \leq 0.9$) are attributed fcc−Ni with PDF−04−0850. Scherrer analysis of the
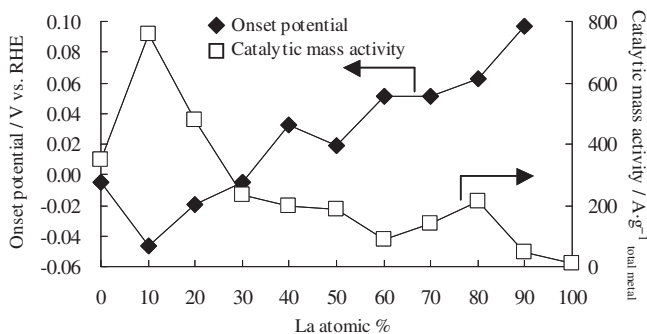
Fig. 2. Relationship between composition of Ni−La and onset potential (left Y axis), mass activity (right Y axis).
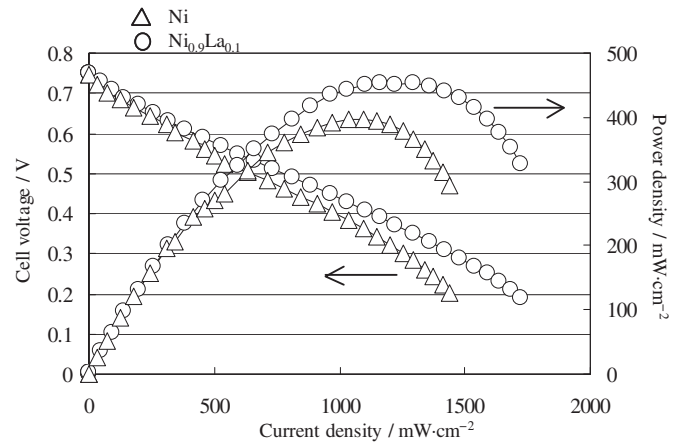
Fig. 3. DHFC MEA tests with Ni (210H, INCO) and $Ni_{0.9}La_{0.1}$ which was synthesized by spray pyrolysis. Loading of anode/cathode = 2.7/0.24 mg cm^{-2}.

Ni peak width suggests that Ni particles have a crystallite size of 21.6 nm. Diffraction peaks for La-oxide were not observed in the La/C and $Ni_{1-x}La_x$/C ($0.1 \leq x \leq 0.9$) samples, either because the La is amorphous or the oxide particles, which have low X-Ray cross sections, are too small to detect by XRD.

3.4. XAFS measurement

XAFS measurements were performed to bridge the bulk-analysis nature of XRD and high spatial resolution of TEM and HVEM. In XAFS the valence state of Ni and La can be estimated from the X-ray absorption near edge structure (XANES) spectrum. Fig. 5a shows the XANES spectrum for Ni K-edge in $Ni_{0.9}La_{0.1}$/C, together with the XANES spectra of Ni foil, $LaNi_5$, and NiO as reference materials. The adsorption edge of Ni K-edge in $LaNi_5$ is shifted toward lower energy compared to the Ni foil in Fig. 5a. This chemical shift of Ni K-edge in $LaNi_5$ compared to Ni foil indicates that Ni in $LaNi_5$ tends to have a slightly negative charge in comparison with the Ni foil, likely because La is an electron-donor. The spectrum also indicates a 0-valent state for the Ni in both $LaNi_5$ and Ni foil. The adsorption edge of Ni in $Ni_{0.9}La_{0.1}$/C shows a significant 1 eV downward chemical shift compared to pure Ni, shown in the Fig. 5a inset, suggesting that the $LaNi_5$, also seen by HVEM, is widespread throughout the sample. This reduced electronic charge on Ni is consistent with improved hydrazine adsorption as determined by DFT [38,39]. The radial structure function for Ni was produced by Fourier transform of the extended X-ray absorption fine structure (EXAFS) oscillations as shown in Fig. 5b. The interatomic distance of the first nearest neighbor shell in the $LaNi_5$ was the same as the Ni foil. For the coordination region from 3 Å to 6 Å the spectra structures for $LaNi_5$ and Ni foil are similar, except for the spectrum intensity. The spectrum for the radial structure function of $Ni_{0.9}La_{0.1}$/C lies between that of $LaNi_5$ and the Ni foil, without the Ni−O peak. The Ni K-edge XAFS measurement thus supports the presence of fcc−Ni core with some hcp−$LaNi_5$ shell structure particles in $Ni_{0.9}La_{0.1}$/C, as is seen by HVEM analysis.

Table 3
Cell performance of prepared $Ni_{0.9}La_{0.1}$ anode catalyst, together with Ni as a reference catalyst.

| Catalyst	Open circuit voltage (V)	Maximum power density (mW cm^{-2})
Ni	0.746	397
$Ni_{0.9}La_{0.1}$	0.751	453
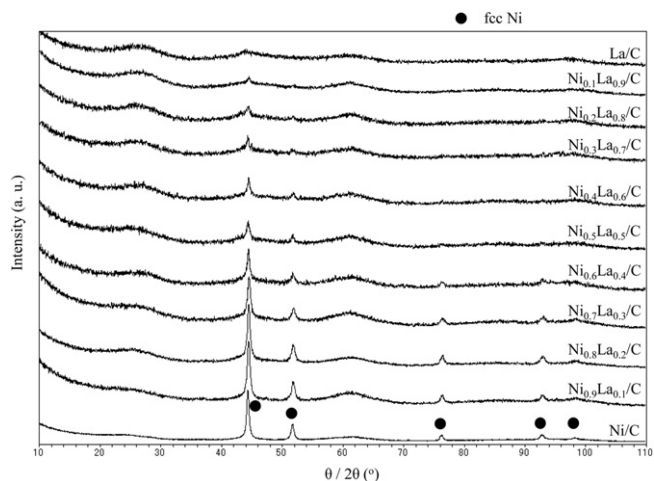
Fig. 4. X-ray diffraction spectra of the Ni/C, La/C, and $Ni_{1-x}La_x/C$ ($0.1 \leq x \leq 0.9$) catalysts.

La L_3-edge XANES and EXAFS spectra of $Ni_{0.9}La_{0.1}/C$, and the reference materials $LaNi_5$, $La_2(CO_3)_3$, and La_2O_3 are shown in Fig. 5c and d, respectively. Both XANES and EXAFS spectra of $Ni_{0.9}La_{0.1}/C$ match the $La_2(CO_3)_3$ spectrum, seemingly conflicting with Ni

K-edge and HVEM analysis that suggest a Ni−$LaNi_5$ core−shell structure for $Ni_{0.9}La_{0.1}/C$. This disparity is easily explained since XAFS is a bulk analysis technique whereas HVEM only analyzes a very small portion of the examined materials. Therefore the majority La in $Ni_{0.9}La_{0.1}/C$ exists as $La_2(CO_3)_3$ when exposed to air, and a minor (less than 10 at %) portion of the total La in $Ni_{0.9}La_{0.1}/C$ can form the inter-metallic alloy ($LaNi_5$) by reacting with Ni on the surface layer of Ni rich particles.

3.5. TEM and HVEM analysis

Fig. 6 shows TEM micrographs of Ni/C, $Ni_{0.9}La_{0.1}/C$, $Ni_{0.6}La_{0.4}/C$, and La/C. The diameter of the metal particles in the Ni/C catalyst ranged from 20 nm to 30 nm as shown in Fig. 6a, in agreement with XRD Scherrer analysis. Meanwhile, the diameter of the dense particles in the La/C catalyst was approximately 5 nm−10 nm as shown Fig. 6d. The low contrast of particles in the La/C sample suggests the La/C particles are oxides or carbonates with a low crystallinity level. The small size of the particles and low level of La-oxides explain the lack of observed La-oxides peaks in the XRD spectra. Fig. 6b−c show that $Ni_{0.9}La_{0.1}/C$ and $Ni_{0.6}La_{0.4}/C$ contain mixtures of the particles found in Ni/C and La/C, likely corresponding to 20−30 nm Ni and 5−10 nm La-oxide particles. Fig. 6e−f similarly show that $Ni_{0.9}La_{0.1}/C$ contains a mix of the two particles types. The elemental
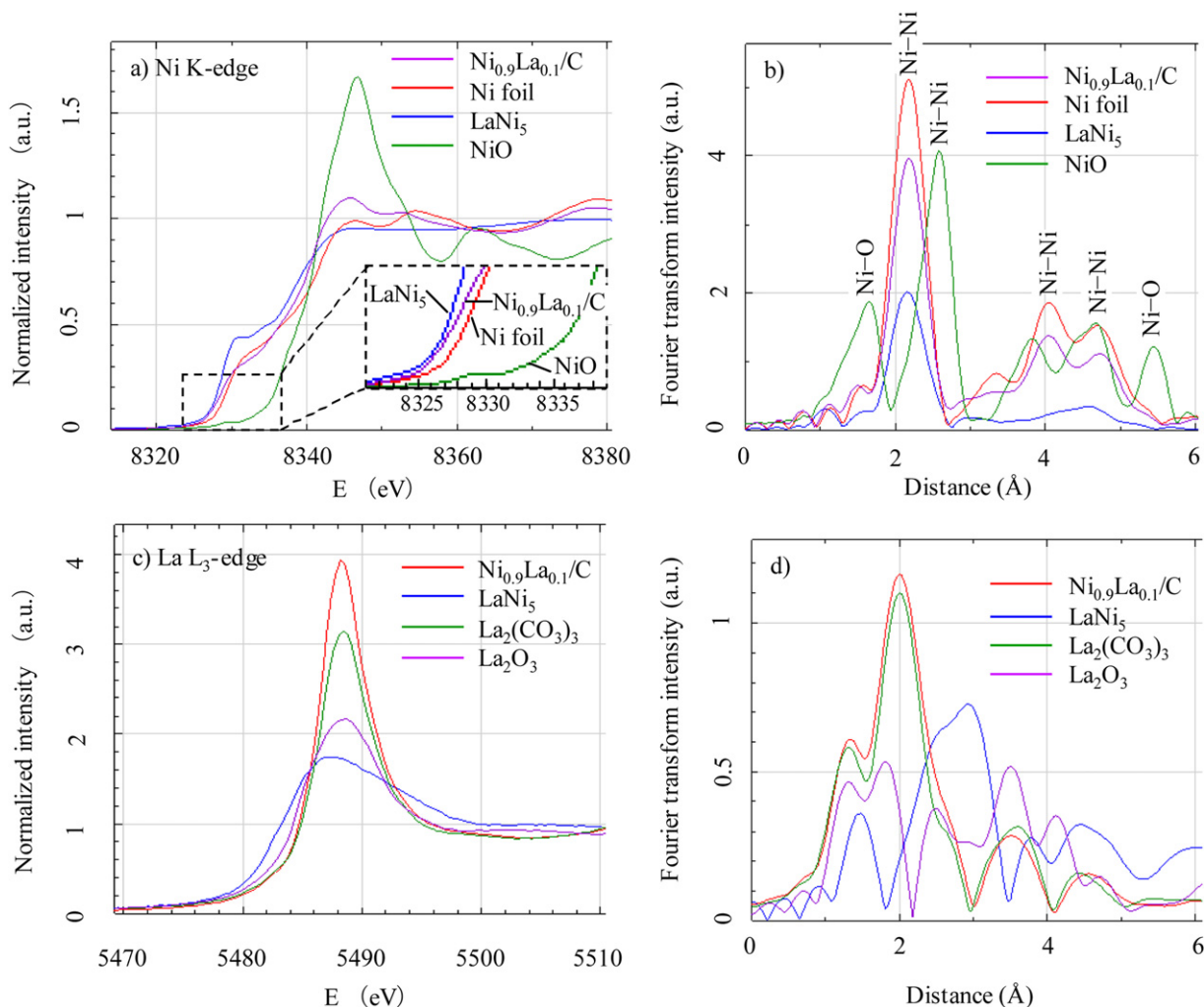
Fig. 5. XAFS data for $Ni_{0.9}La_{0.1}/C$, together with Ni foil, $LaNi_5$, NiO, $La_2(CO_3)_3$, and La_2O_3 as reference materials. (a, c) XANES spectra were measured in transmission mode near the Ni K-edge (a) and La L_3-edge (c). (b, d) The radial structure function around Ni (b) and La (d) were produced as the magnitude of the Fourier transform of the k^2-weighted EXAFS oscillations.
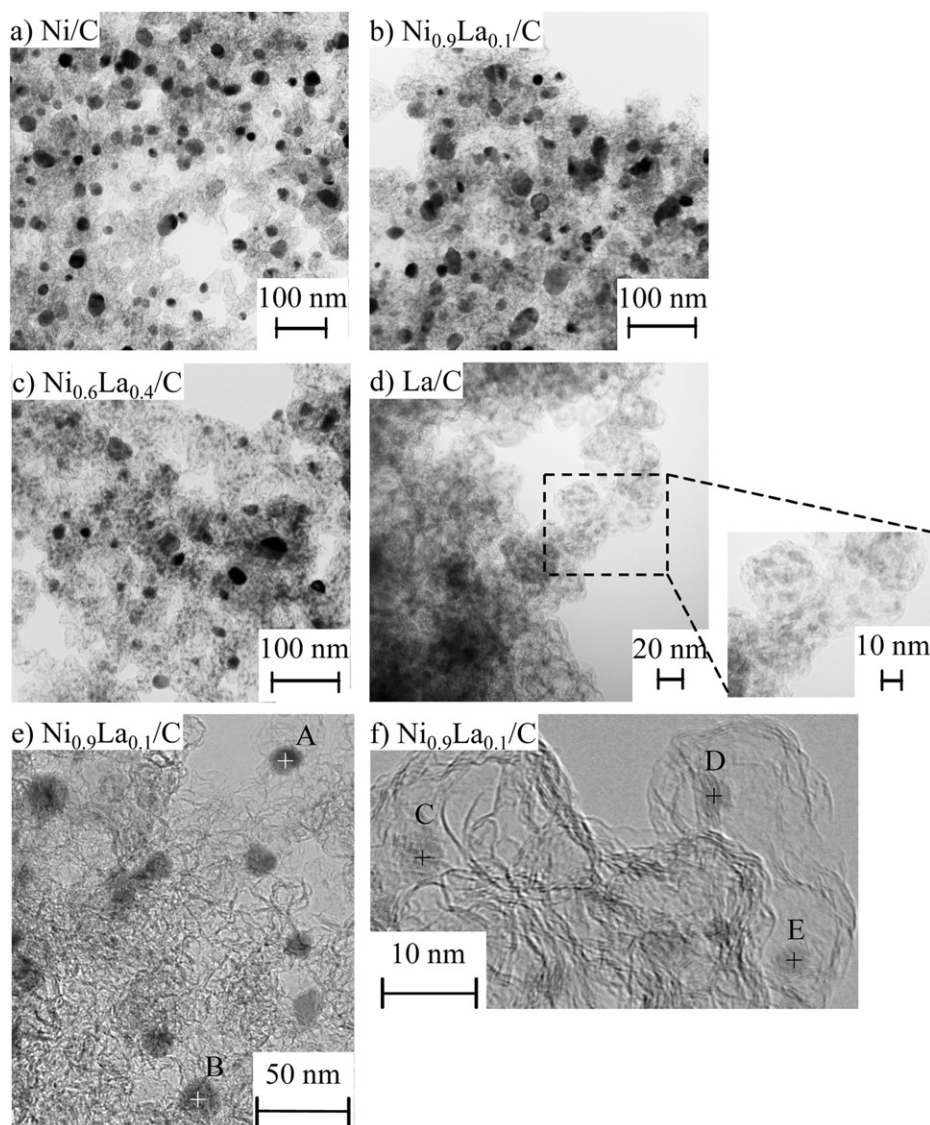
Fig. 6. Low magnification TEM micrographs of (a) Ni/C, (b) $Ni_{0.9}La_{0.1}/C$, (c) $Ni_{0.6}La_{0.4}/C$, and (d) La/C. High magnification of TEM micrographs of (e, f) $Ni_{0.9}La_{0.1}/C$.

composition of the entire view range of Fig. 6b–c was analyzed by EDX. The elemental composition of 5 randomly selected individual metal particles in the $Ni_{0.9}La_{0.1}/C$ imaged in Fig. 6e–f were also analyzed by spot-analysis with EDX. Table 4 summarizes the atomic ratio of Ni–La for the 5 particles designated A–E in Fig. 6e–f. The composition of the entire viewing range of Fig. 6b–c was close to the projected composition of $Ni_{0.9}La_{0.1}/C$ and $Ni_{0.6}La_{0.4}/C$, respectively. However, the composition of different particles in the images

Table 4
EDX analysis of composition of $Ni_{0.9}La_{0.1}/C$ and $Ni_{0.6}La_{0.4}/C$, and EDX spot analysis of composition of $Ni_{0.9}La_{0.1}/C$.

View	Ni atomic %	La atomic %
Fig. 4b	90.0	10.0
Fig. 4c	57.7	42.3
A) In Fig. 4e	98.7	1.3
B) In Fig. 4e	98.9	1.1
C) In Fig. 4f	95.7	4.3
D) In Fig. 4f	28.6	71.4
E) In Fig. 4f	24.1	75.9

is not homogeneous. The composition of Ni/C like particles in $Ni_{0.9}La_{0.1}/C$ as shown in Fig. 6e were Ni rich, and La/C like particles in $Ni_{0.9}La_{0.1}/C$ as shown in Fig. 6f were La rich.

Since the La/C and thus the La particles are inactive for hydrazine oxidation as shown in Fig. 1, we focused on the surface structure of the Ni rich particles in $Ni_{0.9}La_{0.1}/C$ by HVEM. It is important to note that these samples are very difficult to image, as the samples are heavily coated with graphitic carbonaceous material which greatly hinders imaging the shells of the dense metallic particles evident under normal voltage TEM. Therefore HVEM (1000 kV) had to be used for the analysis of the shells, shown in Fig. 7. Fig. 7 shows high resolution TEM (HRTEM) micrographs of the Ni rich particles found in the most active $Ni_{0.9}La_{0.1}/C$ and lower activity $Ni_{0.4}La_{0.6}/C$ catalysts. Inset in the micrographs are Fourier transform (FFT) power spectra for the areas indicated by dotted squares. All particle cores indexed to fcc-Ni. The crystalline structure of the $Ni_{0.9}La_{0.1}/C$ shell indexed to hcp–$LaNi_5$ (see Supplementary information for details; the characterization of surface structure of $Ni_{0.9}La_{0.1}/C$ using HVEM is shown in Supplementary Fig. S1) and the shell of $Ni_{0.4}La_{0.6}/C$ indexed to orthorhombic LaNi, as shown in Fig. 5a and b respectively. Thus the

a) $Ni_{0.9}La_{0.1}/C$

b) $Ni_{0.4}La_{0.6}/C$

2.03 Å
Ni (111)

2.03 Å
Ni (111)

2.10 Å
$LaNi_5$ (200)

2.57 Å
$LaNi_5$ (110)

2.46 Å
$LaNi_5$ ($1\bar{1}0$)

surface

3 nm

2.03 Å
Ni (111)

1.80 Å
Ni (200)

2.03 Å
Ni (111)

2.03 Å
LaNi (200)

1.50 Å
LaNi (241)

2.34 Å
LaNi (041)

surface

1 nm

Fig. 7. HVEM micrographs of surface of (a) $Ni_{0.9}La_{0.1}/C$ and (b) $Ni_{0.4}La_{0.6}/C$. Inset are indexed FFT power spectrum of the areas in the dotted squares.

Ni rich particles are composed of a Ni core, and NiLa intermetallic alloy shell with the shell composition varying with La content. The HVEM analysis therefore suggests that the best performing catalysts are composed of core-shell $Ni_{fcc}-Ni_xL_y$ particles, with the best performing catalyst having what may be a $LaNi_5$ shell. This observed correlation between catalyst surface structure and catalytic performance for hydrazine oxidation is consistent with DFT work by M. K. Agusta et al. where the stability and mechanism of hydrazine adsorption on Ni single crystal surface is shown to depend on the surface structure [38,39]. The hydrazine oxidation of the $Ni_{0.9}La_{0.1}/C$ electrocatalysts below 0 V vs. RHE occurs as shown in Fig. 1. This result indicates that $LaNi_5$ on the surface of Ni rich particles in $Ni_{0.9}La_{0.1}/C$ catalyst directly oxidizes the hydrazine as shown in Table 1. We suppose that $LaNi_5$ contributes to break the N–H bond after hydrazine is adsorbed on the working catalyst surface. While the observation of NiLa alloys under air exposure is unexpected and may be attributed non-statistical nature of TEM, the preceding XAFS analysis also suggests that NiLa alloys are a significant portion of the Ni_xLa_{1-x}/C catalysts.

4. Conclusions

A series of $Ni_{1-x}La_x/C$ catalysts was synthesized, characterized and tested for hydrazine hydrate electro-oxidation in alkaline media. Lanthanum-rich samples performed poorly, while Nickel-rich catalysts performed better. The $Ni_{0.9}La_{0.1}/C$ catalyst showed the highest catalytic activity, with 42 mV improved onset and 2.17 times higher mass activity compared to a similarly made Ni/C. Unsupported $Ni_{0.9}La_{0.1}$ made using spray pyrolysis was then tested in a DHFC MEA, also showing improved activity compared to Nickel. To understand the cause of the improved performance of the $Ni_{1-x}La_x/C$ catalysts XAFS, TEM, and HVEM were used for characterizing the samples. XAFS measurements show a minor, but significant, component of NiLa alloys in the better performing Nickel-rich catalysts. Further, the best performing $Ni_{0.9}La_{0.1}/C$ contained $LaNi_5$, supporting the hypothesized presence of an hcp–$LaNi_5$ shell on the fcc-Ni core particles in the most active $Ni_{0.9}La_{0.1}/C$ catalyst. TEM and HVEM imaging also shows that the most active catalysts contain metallic particles composed of a fcc-Ni core and NiLa shell. The shell composition and structure change with sample composition, so the best performing $Ni_{0.9}La_{0.1}/C$ shell is hcp–$LaNi_5$ while the $Ni_{0.6}La_{0.4}/C$ shell is LaNi.

This study of $Ni_{1-x}La_x/C$ catalysts hydrazine hydrate electro-oxidation in alkaline media NiLa established that a $Ni_{0.9}La_{0.1}/C$ catalyst performs better than Ni or other NiLa alloys. Further a $LaNi_5$ surface layer on the Ni-rich particles in the $Ni_{0.9}La_{0.1}/C$, detected by XAFS and HVEM, may be the cause of the improved hydrazine oxidation observed for this catalyst, which while surprising is consistent with the known hydrogen affinity of $LaNi_5$. Follow up studies using unsupported $Ni_{0.9}La_{0.1}$ made by spray pyrolysis, and which are therefore more amenable to careful characterization are upcoming.

Appendix A. Supplementary data

Supplementary data related to this article can be found at http://dx.doi.org/10.1016/j.jpowsour.2013.01.181.

References

[1] K.D. Snell, A.G. Keenan, Electrochim. Acta 27 (1982) 1683.
[2] X. Ren, M.S. Wilson, S. Gottesfeld, J. Electrochem. Soc. 143 (1996) L12.
[3] N. Maffei, L. Pelletier, J.P. Charland, A. McFarlan, J. Power Sources 140 (2005) 264.
[4] S.C. Amendola, P. Onnerud, M.T. Kelly, P.J. Petillo, S.L. Sharp-Goldman, M. Binder, J. Power Sources 84 (1999) 130.
[5] K. Yamada, K. Yasuda, N. Fujiwara, Z. Siroma, H. Tanaka, Y. Miyazaki, T. Kobayashi, Electrochem. Commun. 5 (2003) 892.
[6] K. Asazawa, K. Yamada, A. Oka, M. Taniguchi, T. Kobayashi, Angew. Chem. Int. Ed. 46 (2007) 8024.
[7] W.X. Yin, Z.P. Li, J.K. Zhu, H.Y. Qin, J. Power Sources 182 (2008) 520.
[8] A. Serov, C. Kwak, Appl. Catal. B: Environ. 98 (2010) 1.
[9] Environmental Health Criteria, vol. 68, IPCS, 1987.
[10] IARC Monographs on the Evaluation of Carcinogenic Risks to Humans, vol. 4 (1974). Suppl. 7, 1987, vol. 71, 1999.
[11] W. Qian, D.P. Wilkinson, J. Shen, H. Wang, J. Zhang, J. Power Sources 154 (2006) 202.
[12] U.B. Demirci, J. Power Sources 169 (2007) 239.
[13] R. Jasinski, Electrochem. Technol. 129 (1965) 3.
[14] S. Karp, L. Meites, J. Am. Chem. Soc. 84 (1962) 906.
[15] G.E. Evans, K.V. Kordesch, Science 158 (1967) 1148.

[16] K. Tamura, T. Kahara, J. Electrochem. Soc. 123 (1976) 776.
[17] Y. Fukumoto, T. Matsunaga, T. Hayashi, Electrochim. Acta 26 (1981) 633.
[18] K. Yamada, K. Asazawa, K. Yasuda, T. Ioroi, H. Tanaka, Y. Miyazaki, T. Kobayashi, J. Power Sources 115 (2003) 236.
[19] K. Yamada, K. Yasuda, H. Tanaka, Y. Miyazaki, T. Kobayashi, J. Power Sources 122 (2003) 132.
[20] K. Asazawa, K. Yamada, H. Tanaka, M. Taniguchi, K. Oguro, J. Power Sources 191 (2009) 362.
[21] G. Gao, D. Guo, C. Wang, H. Li, Electrochem. Commun. 9 (2007) 1582.
[22] E. Granot, B. Filanov, I. Presman, I. Kuras, F. Patolsky, J. Power Sources 204 (2012) 116.
[23] C.-C. Yang, A.S. Kumar, M.-C. Kuo, S.-H. Chien, J.-M. Zen, Anal. Chim. Acta 554 (2005) 66.
[24] K. Asazawa, T. Sakamoto, S. Yamaguchi, H. Fujikawa, H. Tanaka, K. Oguro, J. Electrochem. Soc. 156 (2009) B509.
[25] U. Martinez, K. Asazawa, B. Halevi, T. Olson, B. Kiefer, A.K. Datye, H. Tanaka, P. Atanassov, ECS Trans. 33 (2010) 1673.
[26] U. Martinez, K. Asazawa, B. Halevi, A. Falase, B. Kiefer, A. Serov, M. Padilla, T. Olson, A. Datye, H. Tanaka, P. Atanassov, Phys. Chem. Chem. Phys. 14 (2012) 5512.
[27] J.S. Chinchira, K. Asazawa, T. Sakamoto, K. Yamada, H. Tanaka, P. Strasser, J. Am. Chem. Soc. 133 (2011) 5425.
[28] T. Sakamoto, K. Asazawa, K. Yamada, H. Tanaka, Catal. Today 164 (2011) 181.
[29] L.Q. Ye, Z.P. Li, H.Y. Qin, J.K. Zhu, B.H. Liu, J. Power Sources 196 (2011) 956.
[30] Y. Qingfeng, L. Lei, Y. Wenqiamg, L. Xiaoping, Z. Zhihua, N. Huidong, Rare Met. 29 (2010) 26.
[31] S.J. Lao, H.Y. Qin, L.Q. Ye, B.H. Liu, Z.P. Li, J. Power Sources 195 (2010) 4135.
[32] H. Yang, X. Zhong, Z. Dong, J. Wang, J. Jin, J. Ma, RSC Adv. 2 (2012) 5038.
[33] J.S. Pinter, K.L. Brown, P.A. DeYoung, G.F. Peaslee, Talanta 71 (2007) 1219.
[34] S. Yamazaki, T. Ioroi, K. Tanimoto, K. Yasuda, K. Asazawa, S. Yamaguchi, H. Tanaka, J. Power Sources 204 (2012) 79.
[35] S. Nagasaki, M. Hayashi, Collection of Binary Alloy Phase Diagram, Agune Technical Center, 2001, 195.
[36] K.C. Neyerlin, G. Bugosh, R. Forgie, Z. Liu, P. Strasser, J. Electrochem. Soc. 156 (2009) B363.
[37] N. Hoshi, Y. Asaumi, M. Nakamura, K. Mikita, R. Kajiwara, J. Phys. Chem. C 113 (2009) 16843.
[38] M.K. Agusta, M. David, H. Nakanishi, H. Kasai, Surf. Sci. 604 (2010) 245.
[39] M.K. Agusta, H. Kasai, Surf. Sci. 606 (2012) 766.